

Prediction of biopore and matrix dominated flow from X-ray CT-derived macropore network characteristics

Muhammad Naveed^{1}, Per Moldrup³, Marcel Schaap⁴, Markus Tuller⁴, Ramaprasad Kulkarni^{4,5}, Hans-Jörg Vogel⁶, and Lis Wollesen de Jonge²*

¹Institute of Biological and Environmental Sciences, University of Aberdeen, King's College, Aberdeen AB24 3FX, United Kingdom.

²Department of Agroecology, Faculty of Science and Technology, Aarhus University, Blichers Allé 20, Postbox 50, DK-8830 Tjele, Denmark.

³Department of Civil Engineering, Aalborg University, Sohngaardsholmsvej 57, DK-9000 Aalborg, Denmark.

⁴Department of Soil, Water and Environmental Science, The University of Arizona, 1177 E. 4th Street, Tucson, AZ 85721, United States.

⁵Department of Electrical and Computer Engineering, The University of Arizona, 1230 E Speedway Blvd., Tucson, AZ 85721, United States.

⁶Department of Soil Physics, Helmholtz Center for Environmental Research-UFZ, Theodor Lieser Straße 4, 06120 Halle [Saale], Germany.

***Corresponding Author:**

Muhammad Naveed

Institute of Biological and Environmental Sciences, University of Aberdeen, King's College, Aberdeen AB24 3FX, UK.

E-mail: Muhammad.Naveed@abdn.ac.uk; Phone: [+441224272258](tel:+441224272258)

Abstract

Prediction and modeling of localized flow processes in macropores is of crucial importance for sustaining both soil and water quality. However, currently there are no reliable means to predict preferential flow due to its inherently large spatial variability. The aim of this study was to investigate the predictive performance of previously developed empirical models for both water and air flow and to explore the potential applicability of X-ray Computed Tomography (CT) derived macropore network characteristics. For this purpose, 65 cylindrical soil columns (6 cm diameter and 3.5 cm height) were extracted from the topsoil (5 cm to 8.5 cm depth) in a 15 m \times 15 m grid from an agricultural field located in Silstrup, Denmark. All soil columns were scanned with an industrial X-Ray CT scanner (129 μ m resolution) and later employed for measurement of saturated hydraulic conductivity, air permeability at -30 cm and -100 cm matric potential, and gas diffusivity at -30 cm and -100 cm matric potential. Distribution maps for saturated hydraulic conductivity, air permeability and gas diffusivity reflected no autocorrelation irrespective of soil texture and organic matter content. Existing empirical predictive models for saturated hydraulic conductivity and air permeability showed poor performance, as they were not able to realistically capture macropore flow. The tested empirical model for gas diffusivity predicted measurements at -100 cm matric potential reasonably well, but failed at -30 cm matric potential, particularly for soil columns with biopore-dominated flow. X-ray CT derived macroporosity matched the measured air-filled porosity at -30 cm matric potential well. Many of the CT derived macropore network characteristics were strongly interrelated. Most of the macropore network characteristics were also significantly correlated with saturated hydraulic conductivity, air permeability, and gas diffusivity. The predictive Ahuja et al. (1984) model for saturated hydraulic conductivity, air permeability, and gas diffusivity performed reasonably well when parameterized with novel, X-ray CT derived parameters such as effective percolating macroporosity for biopore-dominated flow and total

macroporosity for matrix-dominated flow. The obtained results further indicate that it is crucially important to discern between matrix-dominated and biopore-dominated flow for accurate prediction of macropore flow from macropore network characteristics.

1. Introduction

The importance of macropore flow for the partitioning of precipitation between runoff and infiltration, for plant water uptake and plant growth, for biogeochemical cycling rates, and for potential risks of ground water contamination is widely recognized (*Iversen et al.*, 2011; *de Jonge et al.*, 2004; *Fox et al.*, 2004; *Moustafa*, 2000). Thus, over the last decade, major research efforts have been devoted to improve the understanding of macropore flow and associated governing parameters, and to develop predictive macropore flow models (*Jarvis*, 2007). Macropore flow and transport refers to the localized and commonly very rapid movement of water and solutes through the soil profile. Macropores resulting from biological activity (root channels, worm holes etc.), geological forces (subsurface erosion, shrinkage and swelling etc.), and agricultural management (e.g., plowing) serve as the main channels for this rapid and long-distance flow and transport of water, air, and contaminants. Macropore flow is largely determined by soil structure and is generally a dominating process in loamy and clayey soils (*Jarvis et al.*, 2009) where large inter-aggregate pores and biopores often act as pathways for rapid flow and transport. The transition from matrix to macropore flow (equilibrium to non-equilibrium) depends on the pore size distribution and pore continuity, and the degree of soil saturation (*Bouma*, 1981). Macropore flow often occurs in pores with equivalent effective cylindrical diameters larger than 0.3 mm, which indicates that the matric potential needs to be close to zero and the water content close to saturation for these pores to be activated (*Jarvis*, 2007).

Soil and crop management practices strongly modify soil structure and thus the extent of macropore flow and transport. *Wang et al.* (2013) and *Gonzalez-Sosa et al.* (2010)

1 studied the impact of land use on the hydraulic properties of the topsoil of the Loess Plateau of
2 China and for a suburban catchment in France, respectively. Both studies have reported greater
3 saturated hydraulic conductivities for forested land, intermediate for permanent pasture, and
4 lower for farmland soils. This is primarily due to the abundance of biota and less disturbance
5 in forests and permanent pastures when compared to cultivated lands (*Naveed et al.*, 2014a;
6 *Norgaard et al.*, 2013; *Pérès et al.*, 2012). Application of animal manure and fertilizers can
7 also influence macropore flow, first by altering soil structure and second by promoting the
8 density of earthworms, particularly deep penetrating anecic worms (*Naveed et al.*, 2014b).
9 Climatic conditions (seasonal temperature and precipitation variations) might also affect soil
10 structure and macropore flow through interactions with physical processes such as cyclic
11 freezing/thawing and wetting/drying (*Hu et al.*, 2012). Due to the complex interactions and the
12 significant number of influencing factors, a large spatial variability of saturated hydraulic
13 conductivity has been reported by several authors (*Wang et al.*, 2013; *Raczkowski et al.*, 2012;
14 *Iversen et al.*, 2011). Therefore, the predictive capabilities of empirical models/pedotransfer
15 functions for saturated hydraulic conductivity are limited because they ignore the effects of key
16 site factors and underestimate the significance of soil structure (*Vereecken et al.*, 2010).
17 Recently, pedotransfer functions for saturated hydraulic conductivity that account for soil
18 structure have been developed, but they are rarely applied due to the complexity of input
19 parameters and the still significant prediction inaccuracies (*Jarvis et al.*, 2013; *Iversen et al.*,
20 2011; *Lilly et al.*, 2008).

21 Along with the prediction of macropore water flow (i.e. saturated hydraulic
22 conductivity), prediction of macropore airflow (i.e. air permeability and diffusivity) is also of
23 essence. Air permeability is a key parameter for the design of soil vapor extraction remediation
24 methods. Air diffusivity is of importance because the availability of oxygen to plant roots via
25 diffusion is a basic factor for plant productivity. Various empirical models have been proposed

1 in the past for the prediction of air permeability (*Chamindu Deepagoda et al., 2011; Kawamoto*
2 *et al., 2006*) and air diffusivity (*Chamindu Deepagoda et al., 2011; Moldrup et al., 2000*).
3 However, none of the above studies have evaluated their applicability after discerning between
4 biopore- and matrix-dominated flow domains.

5 Recent developments in soil imaging techniques not only allow visual observations
6 but also quantification of pore network complexity. Application of X-ray CT provides
7 emerging alternative means for estimating subsurface macropore flow and transport
8 (*Wildenschild and Sheppard, 2013*). Over the last decade, numerous studies about the
9 characterization of macropore structure (i.e. macroporosity, macropore size distribution,
10 volume, surface area, tortuosity, etc.) were conducted with X-Ray CT for different land use
11 and management systems (*Katuwal et al., 2015; Larsbo et al., 2014; Hu et al., 2014; Naveed*
12 *et al., 2013; Vogel et al., 2010; Luo et al., 2010*). However, to date there are only a very few
13 published studies on quantitatively relating macropore network characteristics to the
14 observations of macropore flow. *Katuwal et al. (2015)* found that CT derived macroporosity
15 for the limiting section of a soil column was strongly correlated with air permeability and 5%
16 tracer arrival time. *Larsbo et al. (2014)* reported significant correlations between X-ray CT
17 derived macropore network characteristics and flow and transport parameters. *Paradelo et al.*
18 *(2013)* found that CT derived macroporosity was strongly correlated with saturated hydraulic
19 conductivity, solute dispersivity, and contaminant breakthrough. *Luo et al. (2010)* reported that
20 macroporosity, path number, hydraulic radius, and macropore angle were the most useful X-ray
21 CT derived parameters for predicting macropore flow and transport under saturated conditions.

22 In this study we first evaluate the predictive performance of existing pedotransfer
23 functions/models for saturated hydraulic conductivity, air permeability, and gas diffusivity.
24 While it has been previously demonstrated that water flow in macropores cannot be accurately
25 predicted with empirical models from basic soil properties (*Weynants et al., 2009; Vereecken*

et al., 2010), there is only little published work related to gas diffusivity. Furthermore, existing pedotransfer functions/empirical models do not discern between matrix- and biopore-dominated flow domains, which is of significance for understanding and accurate prediction of preferential flow as demonstrated in the results section. In the second part of this study we derive novel macropore network characteristics from X-ray CT observations for the prediction of saturated hydraulic conductivity, air permeability, and gas diffusivity, which demonstrated their utility for improving accuracy of gas and water flow predictions. The simplest form of the Kozeny-Carman equation proposed by *Ahuja et al.* (1984) is parameterized with novel CT derived parameters such as percolating macroporosity for biopore-dominated flow and total macroporosity for matrix-dominated flow, and improvement of prediction accuracy is discussed.

2. Materials and Methods

2.1 Study site and soil sampling

The 1.69-hectare study site located in Silstrup in northwestern Denmark (56° 55' 56" N, 8°38'44" E) is composed of glacial till, a dominant geological formation covering about 43% of all farmland in Denmark (*Geological Survey of Denmark and Greenland*, 1999). The top meter of the soil is highly fractured and bioturbated, containing 100 to 1000 biopores per m². The field has not been tilled for about 3 years prior to soil sampling. It has been plowed in December 2008 to 23-cm depth and harrowed twice to 5-cm depth in March 2009. Since then the soil was only disturbed when slurry was injected in 10-cm depth in April 2009 and in 5-cm depth in September 2009. A thorough overview of management practices at the study site between 2006 and 2010 is provided in *Norgaard et al.* (2013).

Sixty-five undisturbed cylindrical soil cores (6-cm inner diameter and 3.5-cm height) were extracted from the topsoil (5 cm to 8.5 cm depth) in summer 2012. At the time of sampling the field was cultivated with red fescue (*Festuca rubra* L.). The soil columns were

sampled on a 15 m x 15 m grid with additional 5 sampling locations between grid points (Figure 2). All soil columns were extracted by pushing a customized core sampler with aluminum sampling cylinders into the soil and removing the surrounding material step by step. Extracted soil columns were immediately covered with tight plastic lids, placed in plastic bags, and carefully transported to the laboratory to avoid smearing and compaction effects. The soil columns were stored in an environmentally controlled room at 2 °C until the start of the measurements. In addition, bulk soil samples were collected from each point at the same soil depth for texture and organic carbon analysis.

2.2 X-ray Computed Tomography scanning and analysis

An industrial X-Ray CT scanner (X-Tek HMX225) at the Helmholtz Center for Environmental Research in Halle in Germany was used to scan the intact soil columns at a voltage of 180 kV and a current of 400 μ A. A copper filter was placed between the X-ray source and the soil columns to alleviate beam hardening. The shadow projections (radiographs) were reconstructed with a Feldkamp cone-beam algorithm (*Feldkamp et al.*, 1984) to obtain 16-bit grayscale 3-D data comprised of (500×500×300) voxels at a resolution of 129 μ m (Fig. 1a). For subsequent analysis, the 3-D grayscale volumes were cropped to remove the container wall and disturbed regions on the top and bottom of the sample, numerically corrected for intensity differences caused by beam hardening and other scanning artifacts with a sequential algorithm developed by *Iassonov and Tuller* (2010), and a 3-D median filter (*Jassogne et al.*, 2007) with a radius of 6 voxels was applied to the grayscale volumes to remove noise (Fig. 1b). Though, median filtering is computationally more demanding than conventional smoothing filters, it is less sensitive to outlier values and thus preserve edges. A locally adaptive Bayesian Markov random field (MRF) algorithm (*Iassonov et al.*, 2009; *Kulkarni et al.*, 2012) that was seeded with adaptive K-means clustering (*Chen et al.*, 1998) was used to segment the intensity-corrected and filtered data to distinguish macropores from the soil matrix (Fig. 1c). The

homogeneity parameter β in the MRF model was set to 2. For details of the applied MRF segmentation algorithm, see *Kulkarni et al. (2012)* and *Tuller et al. (2013)*.

The segmented CT-data for each soil column were further analyzed with the Image-J software package (*Rasband, 2011*) to obtain macroporosity, percolating macroporosity, effective percolating macroporosity, macropore specific surface area, macropore hydraulic radius, macropore mean diameter, macropore fractal dimension, macropore global connectivity, and macropore local connectivity (see flowchart depicted in Fig. 1). Three-dimensional pore visualization was conducted with the Image-J plugin 3D viewer. Based on 3D visual observations, soil columns containing percolating biopores (round shaped either formed by roots or earthworms) were separated and labeled as biopore-dominated flow columns; the remaining were labeled as matrix-dominated flow columns (Fig. 1d). The number of pore voxels was determined from the segmented data, and macroporosity (MP) was then calculated as the ratio of the number of pore voxels to the number of total sample voxels (Fig. 1d). The percolating macroporosity (PMP) was calculated based on only the pores that were connected from sample top to bottom by removing all isolated pores (Fig. 1e). All isolated pores were removed with the Image-J plugin “Find Connected Regions”. Effective percolating macroporosity (EPMP) was defined and calculated as the ratio of minimum cross-sectional area of percolating macropores (while moving voxel layer by voxel layer from the top to the bottom of the core) and the cross-sectional area of the soil column (Fig. 1f). Macropore specific surface (MPSSA) area was calculated as the ratio of surface area of macropores and the volume of the soil column (Fig. 1g). This was accomplished with the Image-J plugin “Analyze Particles”. Macropore hydraulic radius (MPHR) was defined as the ratio of macropore volume and macropore surface area (Fig. 1h) applying the Image-J plugin “Analyze Particles”. The macropore mean diameter (MPMD) was estimated with a local 3D thickness algorithm proposed by *Dougherty and Kunzelmann (2007)* and embedded in the Image-J plugin “Bone-

J". This algorithm defines the pore diameter as the diameter of the largest sphere that fits within the pore. The histogram of the thickness map was used for estimating macropore size distribution and macropore mean diameter (Fig. 1i). Macropore fractal dimension (MPFD) was calculated as a measure of the heterogeneity of the spatial distribution of macroporosity with the Image-J plugin "Bone-J" (Fig. 1j). Macropore global connectivity (MPGC) was defined and calculated as the ratio of percolating macroporosity to the total macroporosity of the soil column (Fig. 1k). The macropore local connectivity (MPLC) was estimated with the Image J plugin "Bone-J" (Fig. 1l). MPLC equals 1 if all pores are connected in one percolating cluster and 0 if porosity is fragmented into many clusters of similar size. X-Ray CT derived pore network characteristics for all scanned and analyzed core samples are provided in supplementary Table S1.

[Insert Figure 1](#)

2.3 Soil physical measurements

Soil texture was determined from disturbed soil samples using a combination of wet sieving and the hydrometer method, after passing the sample through a 2-mm sieve. Soil organic carbon was determined with a LECO carbon analyzer (St. Joseph, MI, USA) coupled with an infrared CO₂ detector. A multiplication factor of 1.72 was used to convert soil organic carbon to soil organic matter. The sand, silt, clay and organic matter contents for the 65 investigated samples are listed in supplementary Table S2.

After X-ray CT scanning, air permeability and gas diffusivity at -30 cm and -100 cm matric potentials, and saturated hydraulic conductivity (K_{sat}) were measured on the same columns. The soil columns were placed in a sand box and saturated from the bottom with tap water. After saturation, tension was successively applied to establish matric potentials of -30 cm and -100 cm, respectively. Air permeability (K_a) was then measured with the steady state

method described in *Iversen et al.* (2001) both at -30 cm and -100 cm matric potentials. A pressure of 5 hPa was applied to assure laminar flow during the measurements. The K_a was calculated based on the Darcy equation considering the pressure difference across the soil cores:

$$Q = \frac{K_a \Delta p a_s}{\eta_a L_s} \quad (1)$$

where Q ($L^3 T^{-1}$) is the volumetric flow rate, K_a (L^2) is air permeability, Δp ($M L^{-1} T^{-2}$) is the pressure difference across the column, η ($M L^{-1} T^{-1}$) is dynamic viscosity of air, a_s (L^2) is the cross-sectional area and L_s (L) is the length of the column. Gas diffusivities (D_p/D_0) at -30 cm and -100 cm matric potentials were measured with the one-chamber method developed by *Schjønning et al.* (2013).

After D_p/D_0 measurements, the soil columns were resaturated, and the saturated hydraulic conductivity (K_{sat}) was measured with the constant head method (*Klute and Dirksen*, 1986). All measured flow parameters are provided in supplementary Table S3.

2.4 Modelling

Ahuja et al. (1984) developed a relationship (EPM, effective porosity model) between saturated hydraulic conductivity (K_{sat}) and effective porosity (ϕ_e) based on the generalized Kozeny-Carman equation:

$$K_{sat} \text{ or } K_a \text{ or } D_p/D_0 = A \phi_e^B \quad (3)$$

where K_{sat} is saturated hydraulic conductivity, K_a is air permeability, D_p/D_0 is gas diffusivity, and A and B are empirical constants. *Ahuja et al.* (1984) defined ϕ_e as the total porosity minus the soil volumetric water content at field capacity assumed at a matric potential of -33 kPa. Based on a simple calculation applying the capillary rise equation, this means that ϕ_e is the porosity contributed by pores larger than about 9 μm in diameter. We first parameterized the

original Ahuja *et al.* (1984) model with ϕ_e equivalent to the air-filled porosity at -30 kPa. Then, X-ray CT derived macroporosity (MP) was used for ϕ_e for matrix-dominated flow, and X-ray CT derived effective percolating macroporosity (EPMP) was applied for ϕ_e for biopore-dominated flow. Note that because of the 129 μm resolution of the CT scans, the CT derived parameters MP and EPMP represent significantly larger pores than originally suggested in Ahuja *et al.* (1984). This seems quite reasonable and interesting to test as macropore flow often occurs in pores with equivalent effective cylindrical diameters larger than 300 μm (Jarvis, 2007). Rawls *et al.* (1998) reported that several researchers found the slope A to vary between 1.59 and 3.98 and the intercept to vary between 440 cm d^{-1} and 34,000 cm d^{-1} .

2.5 Statistics

Data collected for soil textural properties and macropore flow parameters were first subjected to classical statistical analysis to obtain descriptive statistics, including minimum, maximum, mean, median, standard deviation, skewness, and coefficient of variation (CV). The degree of spatial variability of soil textural properties and macropore flow parameters was determined with ordinary kriging. The ArcMap 10.1 software (Esri Inc., Redlands, CA, USA) was used to generate contour maps for each measured soil property. Spearman rank order correlation coefficients between macropore network characteristics and macropore flow parameters were calculated with the commercial SigmaPlot 11.0 software package (Systat Software, Inc., San Jose, CA, USA). Selected correlations were also graphically displayed and analyzed with linear, power, or exponential regression models. While the applicability of linear models was evaluated, power or exponential models yielded significantly better results in most cases. The models were only fitted if they were significant at $p < 0.01$.

3. Results and Discussion

3.1. Spatial variability of soil texture, organic matter, and macropore flow parameters

The soil of the study site was classified as sandy loam (*USDA-NRCS Web Soil Survey*, 2010) with clay contents ranging from 14 % to 19 %, and organic matter contents varying from 2.9 % to 3.8 %. Descriptive statistics for all soil textural properties are depicted in Table 1. Clay and sand contents were positively skewed, whereas silt and organic matter contents were negatively skewed. All soil textural properties were slightly variable across the field with coefficients of variation (CV) below 10 %. It has been previously reported that the CV for soil textural properties generally depends on the extent of the study area. For example, *Sharma et al.* (2011) reported a CV for soil textural properties within the range of 20 % to 30 % for a 40 ha agricultural field in New Mexico, while *Wang et al.* (2013) reported a CV within the range of 19 % to 156 % across the Loess Plateau of China ($620 \times 10^3 \text{ km}^2$). Kriged maps indicated that soils with high clay contents (Fig. 2a) were on the north side of the field, whereas soils with high organic matter contents occupied the south side (Fig. 2d). Thus, clay and organic matter gradients run in opposite directions at the study site. Soils with high silt contents (Fig. 2b) were on the western part of the field, whereas soils with high sand contents were on the eastern part (Fig. 2c). Relevant information about the semivariograms for each interpolated map is provided in Table 2.

[Insert Figure 2](#)

Descriptive statistics for saturated hydraulic conductivity (K_{sat}), air permeability (K_a), and gas diffusivity (D_p/D_0) at -30 cm and -100 cm matric potentials are provided in Table 1. Large positive skewness and quite different mean and median values were observed for all five macropore flow parameters. The K_{sat} , K_a , and D_p/D_0 at -30 cm and -100 cm matric potentials showed the largest variations across the study site with a CV ranging from 92 % to 218 %. High CV values were observed due to the presence of biopores in some of the soil columns, while not in others. Renderings of the samples marked as *I*, *II*, *III*, and *IV* in Fig. 2 are depicted in Fig. 3. Samples *I* and *II* are matrix-flow dominated and samples *III* and *IV* are

biopore-flow dominated. Irrespective of the extent of the study area, large variations in K_{sat} were also reported in other studies (e.g., Wang *et al.*, 2013; Sharma *et al.*, 2011; and Iqbal *et al.*, 2005). Kriged maps for K_{sat} , K_a , and D_P/D_0 (Figs. 2e-g) look quite similar with some areas randomly exhibiting a high level of macropore flow while matrix flow dominated in other regions irrespective of soil texture and organic matter content.

[Insert Figure 3](#)

[Insert Table 1](#)

[Insert Table 2](#)

3.2. Predictive performance of empirical models

For many hydrological applications, saturated hydraulic conductivity (K_{sat}) is estimated from more readily available proxy variables such as texture and bulk density. Various empirical models/pedotransfer functions (e.g. Iversen *et al.*, 2011; Jarvis *et al.*, 2009; Schaap *et al.*, 2001; Wösten *et al.*, 1999; Revil and Cathles, 1999) have been previously proposed for predicting saturated hydraulic conductivity. We have observed poor predictive performance of empirical K_{sat} models such as proposed by Revil and Cathles (1999) and Schaap *et al.* (2001) (Fig. 4) and for models proposed by Wösten *et al.* (1999), Vereecken *et al.* (1989), and Cosby *et al.* (1984) (not shown). While the measured saturated hydraulic conductivities span over five orders of magnitude due to the presence of a wide range of macro- and biopores in the core samples, model predictions yielded a very narrow K_{sat} range (Fig. 4). The primary reason for the failure of existing empirical models/pedotransfer functions is that they only consider soil texture and bulk density, and thus are not able to realistically capture macropore flow, particularly for highly structured and bioturbated soils. In general, empirical models over-predicted K_{sat} in case of matrix flow (empty symbols), while they under-predicted K_{sat} for soil columns with biopore flow (filled symbols). Because results were obtained for samples of

1 limited size from the A-horizon, it should be noted that for larger scales the structural
2 characteristics and associated flow parameters, especially the parameters related to pore
3 connectivity, might change.

4 Insert Figure 4

5 Over the last two decades, efforts have also been devoted to the development of
6 empirical models for the prediction of air permeability (K_a) (*Moldrup et al., 1998; Kawamoto*
7 *et al., 2006; Chamindu Deepagoda et al., 2011*). We have tested the predictive performance of
8 the recently developed density-corrected K_a model (*Chamindu Deepagoda et al., 2011*) as
9 shown in Figures 5a and 5b. The density-corrected K_a model performed reasonably well for
10 soils with low K_a values (some of the columns with matrix-dominated flow), but completely
11 failed for soils with greater K_a values, especially in the presence of continuous structural cracks
12 or biopores. Starting with *Buckingham (1904)* a more rigorous effort has been made in the
13 previous century to develop empirical models for the prediction of gas diffusivity (*Chamindu*
14 *Deepagoda et al., 2011*). The tested WLR-Marshall model (*Moldrup et al., 2000*) predicted gas
15 diffusivity reasonably well for soil samples associated with matrix flow and underestimated
16 gas diffusivity for soil samples with biopore flow at -30 cm matric potential (Fig. 5c). This
17 indicates that preferential diffusive flow occurs at greater matric potentials close to saturation
18 even though gas diffusivity is a concentration-driven gas transport parameter. However, at -
19 100 cm matric potential, the WLR-Marshall model (*Moldrup et al., 2000*) predicted gas
20 diffusivity well for all soil samples irrespective of matrix or biopore flow (Fig. 5d).

21 Insert Figure 5

3.3. Correlations between macropore flow parameters and macropore network characteristics

The CT-derived macroporosity and the physically measured air-filled porosity at -30 cm matric potential are in good agreement as shown in Fig. 6. At -30 cm matric potential, all pores with diameters larger than 100 μm should have drained according to the capillary-rise equation. This indicates that the physically measured air-filled porosity at -30 cm matric potential (pore diameter > 100 μm) should be greater than the X-ray CT derived macroporosity (resolution = 129 μm). However, this is only true when assuming a parallel bundle of capillary tubes, which is not a realistic assumption for natural soils. Due to the ink-bottle effect a considerable volume of pores with diameters > 100 μm are expected to be water filled after drainage at a matric potential of -30 cm. Hence, no perfect match between the CT-measured morphological pore size and the hydraulic pore size estimated with the capillary-rise equation should be expected (Vogel, 2000). The observed agreement between the two measures is reasonable and confirms the applicability of the applied image segmentation method (Fig. 6). However, it must be noted that different image segmentation methods can result in quite different macroporosity values if the CT image quality is bad, i.e. there is a lot of noise and partial volume effect as shown in Naveed (2014).

Insert Figure 6

Spearman rank order correlation analysis for macropore flow parameters and macropore network characteristics was performed for all soil columns (Fig. 7a), for soil columns with biopore(s) connected from the top to the bottom (Fig. 7b), and for soil columns with inter-aggregate macropores or disconnected biopores (Fig. 7c). Many of the CT-derived macropore network characteristics were strongly correlated (Fig. 7). This is because large macroporosity is associated with large macropore surface area and better connectivity of macropores. This is in agreement with other recent studies (e.g., Katuwal *et al.*, 2015 and

Larsbo *et al.*, 2014). The macropore mean diameter and hydraulic radius were however poorly correlated with other macropore network characteristics. Significant spearman rank order correlations were also observed between macropore flow parameters and most of the CT-derived macropore network characteristics (Fig. 7). X-ray CT derived macroporosity was strongly correlated with macropore flow parameters for all three categories of soil samples (Figs. 7a, 7b, and 7c). Very strong correlations were observed between effective percolating macroporosity (EPMP) and macropore flow parameters for the soil columns with biopores connected from the top to the bottom (Fig. 7b). Macropore hydraulic radius and macropore mean diameter were significantly correlated with macropore flow parameters for the soil columns associated with biopore-dominated flow (Fig. 7b), whereas poorly correlated for soil columns associated with matrix-dominated flow (Fig. 7c). These findings are in agreement with Elliot *et al.* (2010) and Quinton *et al.* (2008). Both macropore global and local connectivity were poorly correlated with macropore flow parameters for the soil columns associated with biopore-dominated flow (Fig. 7b), whereas significantly correlated for the soil columns associated with matrix-dominated flow (Fig. 7c). This makes sense as biopore flow is mainly governed by the largest biopore present in the soil column, whereas matrix flow is mainly controlled by the pore size distribution and connectivity of pores.

Insert Figure 7

Selected correlations were graphically displayed and analyzed with linear, power, and exponential regression models. The later were superior to linear models in most cases as shown in Figure 8. The saturated hydraulic conductivity (K_{sat}) was plotted as a function of CT-derived macroporosity (8a). Two distinct branches were observed for lower macroporosity values, which approach towards a single branch with increasing CT derived macroporosity. The upper branch with greater conductivities comprises core samples with one or more biopores

connected from top to bottom that mainly govern fluid flow (filled symbols). Samples *III* and *IV* marked in Figure 8a and shown in Figure 3 are members of this branch. The lower branch consists of core samples with fluid mainly flowing through inter-aggregate and textural pores (empty symbols). Samples *I* and *II* marked in Figure 8a and shown in Figure 3 are members of this branch. Distinct significant power regressions were observed between K_{sat} and macroporosity for these two categories of the soil columns (Fig. 8a). This suggests that biopore-dominated and matrix-dominated flow columns should be discerned as an initial step prior to studying the relationships between macropore flow and CT-derived macroporosity. Both *Paradelo et al.* (2013) and *Luo et al.* (2010) found similar relationships between saturated hydraulic conductivity and CT derived macroporosity with R^2 ranging from 0.50 to 0.60. A stronger power regression was observed when K_{sat} was plotted as a function of the effective percolating macroporosity (R^2 increased from 0.43 to 0.76), for the soil columns associated with biopore-dominated flow (Fig. 8b, filled symbols), but this is not the case for the soil columns with matrix-dominated flow (Fig. 8b, empty symbols). Significant power regressions were observed between K_{sat} and macropore mean diameter (Fig. 8c). Weak, but significant power regression was observed between K_{sat} and macropore local connectivity for only those soil columns associated with matrix-dominated flow as shown in Figure 8d. No significant regression was observed between K_{sat} and macropore local connectivity for the soil samples associated with biopore-dominated flow (Fig. 8d, filled symbols). A potential explanation for this observation is that the Euler number that is the basis for macropore local connectivity calculations does not account for continuity of the pores from top to bottom.

Air permeability at -30 cm matric potential, K_a (-30), was plotted as a function of macroporosity as shown in Figure 8e. Distinct significant power regressions were observed for the two categories of soil columns, i.e. columns with biopore-dominated flow and with matrix-dominated flow (Fig. 8e). Similar to K_{sat} , the power regression was significantly improved (R^2

increased from 0.49 to 0.80) when $K_a(-30)$ was plotted as a function of effective percolating macroporosity instead of total macroporosity for the soil columns associated with biopore-dominated flow (Fig. 8f, filled symbols). A significant power regression was observed between $K_a(-30)$ and macropore mean diameter for the soil columns with biopore-dominated flow while no significant regression was observed between $K_a(-30)$ and macropore mean diameter for the soil columns with matrix-dominated flow (Fig. 8g). In contrary, significant power regressions were observed between $K_a(-30)$ and macropore local connectivity for soil columns associated with matrix-dominated flow while no significant regression was observed for soil samples associated with biopore-dominated flow (Fig. 8h). Similar power regressions were also observed for $K_a(-100)$ as a function of macroporosity, effective percolating macroporosity, macropore mean diameter, and macropore local connectivity as shown in Figures 8i, 8j, 8k, and 8l, respectively.

Figures 8m and 8n showed significant power regressions when gas diffusivity at -30 cm matric potential, $D_p/D_0(-30)$, was plotted against macroporosity and effective percolating macroporosity, respectively. Distinct significant power regressions observed for soil columns associated with biopore-dominated flow and matrix-dominated flow reflect that preferential diffusive flow occurred at -30 cm matric potential. However, at -100 cm matric potential, a single regression significantly described both types of data associated with biopore flow and matrix flow as shown in Figures 8q and 8r. This indicates that no preferential diffusive flow occurred at and below -100 cm matric potentials. Both $D_p/D_0(-30)$ and $D_p/D_0(-100)$ showed insignificant regressions when plotted as a function of macropore mean diameter for both categories of soil samples (Figs. 8o and 8s). Significant power regressions were observed when $D_p/D_0(-30)$ and $D_p/D_0(-100)$ were plotted as a function of macropore local connectivity for both sets of soil columns associated with matrix flow and biopore flow (Figs 8p and 8t). This

is expected as D_p/D_0 is a concentration-driven gas transport parameter mainly controlled by total air-filled pore space and its connectivity, and not by the pore size (Moldrup *et al.*, 2000).

Insert Figure 8

3.4. Modeling saturated hydraulic conductivity, air permeability and diffusivity

Saturated hydraulic conductivity, air permeability at -30 cm and -100 cm matric potentials, and gas diffusivity at -30 cm and -100 cm matric potentials were modelled with the simplified form of the Kozeny-Carman equation presented in Ahuja *et al.* (1984). First, we have tested the predictive performance of the original Ahuja *et al.* (1984) model with air-filled porosity at -30 kPa as the effective porosity (Fig. 9, red empty symbols). Then, we have modified the original equation with novel CT derived input parameters. The effective porosity in the original model was replaced with the CT derived total macroporosity (MP) in case of matrix-dominated flow (Fig. 9, black empty symbols), and with the effective percolating macroporosity (EPMP) in case of biopore-dominated flow (Fig. 9, black filled symbols). The empirical fitting parameters (A and B) for saturated hydraulic conductivity, air permeability at -30 cm and -100 cm matric potentials, and gas diffusivity at -30 cm and -100 cm matric potentials are provided in Table 3. The 1:1 plots of measured and predicted saturated hydraulic conductivity, air permeability, and gas diffusivity are shown in Figure 9. From Figure 9 it is obvious that predictions with the Ahuja *et al.* (1984) model with novel input data from X-ray CT analysis are very reasonable and yielded better results than the conventionally parameterized Ahuja *et al.* (1984) model. This indicates that X-ray CT derived macropore characteristics (MP and EPMP) at 129- μm resolution are quite useful for predicting macropore flow. However, discerning between biopore- and matrix-dominated flows are prerequisite. The predictive capability of the proposed modelling framework requires further independent validation for different soil types

to confirm the values/ranges for empirical constants A and B for saturated hydraulic conductivity, air permeability, and gas diffusivity.

[Insert Figure 9](#)

[Insert Table 3](#)

4. Conclusions and Perspective

1. While soil textural properties exhibited small spatial variability across the study site with a $CV < 10\%$, the macropore flow parameters saturated hydraulic conductivity, air permeability, and gas diffusivity, showed large spatial variability across the field with a $CV > 100\%$.
2. Predictive performance of existing empirical models/pedotransfer functions for saturated hydraulic conductivity and air permeability at -30 cm and -100 cm matric potentials was unsatisfactory. For saturated hydraulic conductivity, existing empirical models over predicted for cases with matrix-dominated flow and under predicted for cases with biopore-dominated flow. With regard to air permeability, empirical models predicted matrix-dominated flow reasonably well, whereas significant under predictions were observed for cases with biopore-dominated flow. The tested empirical model for the prediction of gas diffusivity performed well at -100 cm matric potential, while it failed at -30 cm matric potential, particularly for the soil columns that contained biopores that were connected from the sample top to the sample bottom (i.e. biopore flow dominated samples).
3. Significant Spearman's Rank correlations were observed between CT-derived macropore network characteristics and macropore flow parameters. These correlations were further improved when the soil columns were separated into matrix-dominated and biopore-dominated flow columns. The predictive performance of the Ahuja *et al.* (1984) model with novel input parameters, namely X-ray CT derived effective percolating macroporosity

(EPMP) for biopore-dominated flow and total macroporosity (MP) for matrix-dominated flow, was significantly improved. However, further studies for different soil textures are required to confirm the values/ranges of the empirical *Ahuja et al.* (1984) A and B model parameters for accurate predictions of saturated hydraulic conductivity, air permeability, and gas diffusivity.

The rapid development of advanced CT-image segmentation and analysis tools in conjunction with computational fluid dynamics provide promising future means to simulate the dynamics of flow and transport directly with CT derived macropore networks as boundaries. One method particularly suitable for simulating macropore flow and transport based on X-ray CT data is the lattice Boltzmann method (LBM). Most of the studies to date that applied the LBM for simulating flow and transport based on CT-data were for granular porous media (glass beads/sand) and fractured rocks, and not for natural field soil samples. The strong correlations between macropore flow parameters and X-ray CT derived macropore network characteristics observed in this study suggest that lattice Boltzmann flow and transport simulations based on X-ray CT images is a promising avenue for future research.

Authors Contributions

Muhammad Naveed, Per Moldrup, Lis Wollesen de Jonge, and Markus Tuller designed the study and wrote the manuscript. Marcel Schaap and Hans-Jörg Vogel assisted with X-ray CT scanning and analysis. Ramaparsad Kulkarni performed image segmentation. All authors contributed to the manuscript with comments and suggestions throughout the writing process.

Acknowledgements

The technical assistance of Stig T. Rasmussen, Bodil B. Christensen, and Michael Koppelgaard is gratefully acknowledged. The study was part of the Soil Infrastructure, Interfaces, and Translocation Processes in Inner Space (Soil-it-is) project, which is funded by the Danish Research Council for Technology and Production Sciences.

References

- Ahuja, L.R., Naney, J.W., Green, R.E., Nielsen, D.R.: Macroporosity to characterize spatial variability of hydraulic conductivity and effects of land management, *Soil Sci. Soc. Am. J.*, 48 (4), 699-702, 1984.
- Bouma, J.: Comments on micro- meso- and macroporosity of soil, *Soil Sci. Soc. Am. J.*, 45, 1244-1245, 1981.
- Buckingham, E.: Contributions to our knowledge of the aerations of soils. *Bur. Soil Bull.* 25. U.S. Gov. Print. Office, Washington, DC, 1904.
- Chamindu Deepagoda, T.K.K., Moldrup, P., de Jonge, L.W., Kawamoto, K., Komatsu, T.: Density-corrected models for gas diffusivity and air permeability in unsaturated soil, *Vadose Zone J.*, 10, 226-238, 2011.

- 1 Chen, C.W., Luo, J., and Parker, K.J.: Image segmentation via adaptive K-mean clustering and
2 knowledge-based morphological operations with biomedical applications. IEEE
3 Trans. Image Process. 7:1673–1683, 1998.
- 4 Cosby, B. J., Hornberger, G. M., Clapp, R.B., and Ginn T.R.: A statistical exploration of the
5 relationships of soil moisture characteristics to the physical properties of soils,
6 Water Resour. Res., 20: 682-690, 1984.
- 7 de Jonge, L.W., Moldrup, P., Rubaek, G.H., Schelde, K., and Djurhuus, J.: Particle leaching
8 and particle-facilitated transport of phosphorus at field scale, Vadose Zone J., 3,
9 462-470, 2004.
- 10 Dougherty, R., and Kunzelmann, K.: Computing local thickness of 3D structures with Image J,
11 Microsc. Microanal., 13, 1678-1679, 2007.
- 12 Elliot, T.R., Reynolds, W.D., and Heck, R.J.: Use of existing pore models and X-ray computed
13 tomography to predict saturated soil hydraulic conductivity, Geoderma, 156, 133-
14 142, 2010.
- 15 Feldkamp, L.A., Davis, L.C., and Kress, J.W.: Practical cone-beam algorithm, J. Opt. Soc.
16 Am., A1, 612–619, 1984.
- 17 Fox, G.A., Malone, R., Sabbagh, G.J., and Rojas, K.: Interrelationship of macropores and
18 subsurface drainage for conservative tracer and pesticide transport, J. Environ.
19 Qual., 33, 2281-2289, 2004.
- 20 Geological Survey of Denmark and Greenland: Digitalt kort over Danmarks jordarter
21 1:200000; GEUS rapport 1999/47 (in Danish), Geological Survey of Denmark
22 and Greenland, Copenhagen, Denmark, 1999.

- 1 Gonzalez-Sosa, E., Braud, I., Dehotin, J., Lassabatere, L., Angulo-Jaramillo, R., Lagouy, M.,
2 Branger, F., Jacqueminet, C., Kermadi, S., and Michel, K.: Impact of land use on
3 the hydraulic properties of the topsoil in a small French catchment, *Hydrol.*
4 *Process.*, 24, 2382-2399, 2010.
- 5 Hu, Y., Feng, J., Yang, T., and Wang, C.: A new method to characterize the spatial structure
6 of soil macropore networks in effects of cultivation using computed tomography,
7 *Hydrol. Process.*, 28, 3419-3431, 2014.
- 8 Hu, W., Shao, M.A., and Si, B.C.: Seasonal changes in surface bulk density and saturated
9 hydraulic conductivity of natural landscapes, *Eur. J. Soil Sci.*, 63, 820-830, 2012.
- 10 Iassonov, P., Gebrenegus, T., and Tuller, M.: Segmentation of X-ray computed tomography
11 images of porous materials: A crucial step for characterization and quantitative
12 analysis of pore structures, *Water Resour. Res.*, 45(9), W09415, 2009.
- 13 Iassonov, P., and Tuller, M.: Application of segmentation for correction of intensity bias in X-
14 ray computed tomography images, *Vadose Zone J.*, 9, 187–191, 2010.
- 15 Iqbal, J., Thomasson, J.A., Jenkins, J.N., Owens, P.R., and Whisler, F.D.: Spatial variability
16 analysis of soil physical properties of alluvial soils, *Soil Sci. Soc. Am. J.*, 69(4),
17 1338-1350, 2005.
- 18 Iversen, B.V., Børgesen, C.D., Lægdsmand, M., Greve, M.H., Heckrath, G., and Kjærgaard,
19 C.: Risk predicting of macropore flow using pedotransfer functions, textural
20 maps, and modeling, *Vadose Zone J.*, 10, 1185-1195, 2011.
- 21 Iversen, B.V., Schjønning, P., Poulsen, T.G., and Moldrup, P.: In situ, on-site and laboratory
22 measurements of soil air permeability: Boundary conditions and measurement
23 scale, *Soil Sci.*, 166, 97-106, 2001.

- 1 Jarvis, N., Koestel, J., Messing, I., Moeys, J., and Lindahl, A.: Influence of soil, land use and
2 climate factors on the hydraulic conductivity of soil, *Hydrol. Earth Syst. Sc.*, 17,
3 5185-5195, 2013.
- 4 Jarvis, N.J., Moeys, J., Hollis, J.M., Reichenberger, S., Lindahl, A.M.L., and Dubus, I.G.: A
5 conceptual model of soil susceptibility to macropore flow, *Vadose Zone J.*, 8,
6 902–910, 2009.
- 7 Jarvis, N.J.: A review of non-equilibrium water flow and solute transport in soil macropores:
8 Principles, controlling factors and consequences for water quality, *Eur. J. Soil*
9 *Sci.*, 58, 523–546, 2007.
- 10 Jassogne, L., McNeill, A., and Chittleborough, D.: 3D visualization and analysis of macro- and
11 meso-porosity of the upper horizons of sodic, texture-contrast soil, *Eur. J. Soil*
12 *Sci.*, 58, 589–598, 2007.
- 13 Katuwal, S., Nørgaard, T., Moldrup, P., Lamandé, M., Wildenschild, D., and de Jonge, L.W.:
14 Linking air and water transport in intact soils to macropore characteristics inferred
15 from X-ray computed tomography, *Geoderma*, 237–238, 9–20, 2015.
- 16 Kawamoto, K., Moldrup, P., Schjønning, P., Iversen, B.V., Komatsu, T., and Rolston, D.E.:
17 Gas transport parameters in the vadose zone: Development and test of power-law
18 models for air permeability, *Vadose Zone J.*, 5, 1205-1215, 2006.
- 19 Klute, A., and Dirksen, C.: Hydraulic conductivity and diffusivity: Laboratory methods. In
20 *Methods of Soil Analysis, Part 1, 2nd Ed. Physical and Mineralogical Methods*. A
21 Klute (ed.). ASA-SSSA, Madison, WI, 687-734, 1986.
- 22 Kulkarni, R., Tuller, M., Fink, W., and Wildenschild, D.: Three-dimensional multiphase
23 segmentation of X-ray CT data of porous materials using a Bayesian Markov
24 random field framework, *Vadose Zone J.*, doi:10.2136/vzj2011.0082, 2012.

- 1 Larsbo, M., Koestel, J., and Jarvis, N.: Relations between macropore network characteristics
2 and the degree of preferential solute transport, *Hydrol. Earth Syst. Sc.*, 18, 5255-
3 5269, 2014.
- 4 Lilly, A., Nemes, A., Rawls, W.J., and Pachepsky, Y.A.: Probabilistic approach to the
5 identification of input variables to estimate hydraulic conductivity, *Soil Sci. Soc.*
6 *Am. J.*, 72, 16-24, 2008.
- 7 Luo, L., Lin, H., and Schmidt, J.: Quantitative relationships between soil macropore
8 characteristics and preferential flow and transport, *Soil Sci. Soc. Am. J.*, 74, 1929-
9 1937, 2010.
- 10 Moldrup, P., Olesen, T., Gamst, J., Schjønning, P., Yamaguchi, T., and Rolston, D.E.:
11 Predicting the gas diffusion coefficient in repacked soil: Water induced linear
12 reduction model. *Soil Sci. Soc. Am. J.*, 64:1588–1594, 2000.
- 13 Moldrup, P., Poulsen, T.G., Schjønning, P., Olsen, T., and Yamaguchi, T.: Gas permeability in
14 undisturbed soils: Measurements and predictive models, *Soil Sci.*, 163, 180-189,
15 1998.
- 16 Moustafa, M.M.: A geostatistical approach to optimize the determination of saturated hydraulic
17 conductivity for large-scale subsurface drainage design in Egypt, *Agr. Water*
18 *Manage.*, 42(3), 291-312, 2000.
- 19 Naveed, M., Moldrup, P., Arthur, E., Holmstrup, M., Nicolaisen, M., Tuller, M., Herath, L.,
20 Hamamoto, S., Kawamoto, K., Komatsu, T., Vogel, H-J., and de Jonge, L.W.:
21 Simultaneous Loss of Soil Biodiversity and Functions Along a Copper
22 Contamination Gradient: When Soil Goes to Sleep, *Soil Sci. Soc. Am. J.*, 78,
23 1239-1250, 2014a.

1 Naveed, M., Moldrup, P., Vogel, H-J., Lamandé, M., Wildenschild, D., Tuller, M., and de
2 Jonge, L.W.: Impact of long-term fertilization practice on soil structure evolution,
3 *Geoderma*, 217-218, 181-189, 2014b.

4 Naveed, M.: Revealing soil architecture and quality: Linking state-of-the-art soil
5 biophysicochemical measurements, visualizations, and simulations. PhD thesis,
6 Aarhus University, 2014.

7 Naveed, M., Moldrup, P., Arthur, E., Wildenschild, D., Eden, M., Lamandé, M., Vogel, H-J.,
8 and de Jonge, L.W.: Revealing soil structure and functional macroporosity along
9 a clay gradient using X-ray computed tomography, *Soil Sci. Soc. Am. J.*, 77, 403–
10 411, 2013.

11 Norgaard, T., Moldrup, P., Olesen, P., Vendelboe, A.L., Iversen, B.V., Greve, M.H., Kjaer, J.,
12 and de Jonge, L.W.: Comparative mapping of soil physical-chemical and
13 structural parameters at field scale to identify zones of enhanced leaching risk, *J.*
14 *Environ. Qual.*, 42, 271-283, 2013.

15 Paradelo, M., Moldrup, P., Arthur, E., Naveed, M., Holmstrup, M., López-Periago, J.E., and
16 de Jonge, L.W.: Effects of Past Copper Contamination and Soil Structure on
17 Copper Leaching from Soil, *J. Environ. Qual.*, 42(6), 1852-1862, 2013.

18 Pérèsa, G., Bellidoa, A., Curmib, P., Marmonierc, P., and Cluzeaua, D.: Relationships between
19 earthworm communities and burrow numbers under different land use systems,
20 *Pedobiologia*, 54, 37-44, 2012.

21 Quinton, W.L., Hayashi, M., and Carey, S.K.: Peat hydraulic conductivity in cold regions and
22 its relation to pore size and geometry, *Hydrol. Process.*, 22, 2829-2837, 2008.

23 Rasband, W.S.: Image-J, U.S. National Institutes of Health, Bethesda, Maryland, USA, 2011.

- Raczkowski, C.W., Mueller, J.P., Busscher, W.J., Bell, M.C., and McGraw, M.L.: Soil physical properties of agricultural systems in a large-scale study, *Soil Till. Res.*, 119, 50-59, 2012.
- Rawls, W.J., Gimenez, D., and Grossman, R.: Use of soil texture, bulk density and slope of the water retention curve to predict saturated hydraulic conductivity. *Trans. ASAE*, 41, 983-988, 1998.
- Revil, A., and Cathles, L.M.: Permeability of shaly sands, *Water Resour. Res.*, 35, 651-662, 1999.
- Schaap, M.G., Leij, F.L., and van Genuchten, M.T.: Rosetta: A computer program for estimating soil hydraulic parameters with hierarchical pedotransfer functions, *J. Hydrol.*, 251(3-4), 163-176, 2001.
- Schjønning, P., Eden, M., Moldrup, P., and de Jonge, L.W.: Two-chamber, two-gas and one-chamber, one-gas methods for measuring the soil-gas diffusion coefficient: Validation and inter-calibration. *Soil Sci. Soc. Am. J.*, 77, 729-744, 2013.
- Sharma, P., Shukla, M.K., and Mexal, J.G.: Spatial variability of soil properties in agricultural fields of Southern New Mexico, *Soil Sci.*, 176, 288-302, 2011.
- Tuller, M., Kulkarni, R., and Fink, W.: Segmentation of X-ray CT data of porous materials: A review of global and locally adaptive algorithms. In: S.H. Anderson and J.W. Hopmans, editors, *Soil–water–root processes: Advances in tomography and imaging*. SSSA Spec. Publ. 61. SSSA, Madison, WI, p. 157–182, 2013.
- USDA-NRCS Web Soil Survey, 2010.
- Available from: <http://websoilsurvey.nrcs.usda.gov/app/WebSoilSurvey.aspx>.
- Vereecken, H., Weynants, M., Javaux, M., Pachepsky, Y., Schaap, M.G., and van Genuchten M.T.: Using pedotransfer functions to estimate the van Genuchten-Mualem soil hydraulic properties: a review, *Vadose Zone J.*, 9, 795-820, 2010.

- Vereecken, H., Maes, J., Feyen, J., and Darius, P.: Estimating the soil moisture retention characteristic from texture, bulk density, and carbon content, *Soil Sci*, 148, 389-403, 1989.
- Vogel, H-J., Weller, U., and Schlüter, S.: Quantification of soil structure based on Minkowski functions, *Comput. Geosci.*, 36(10), 1236-1245, 2010.
- Vogel, H-J.: A numerical experiment on pore size, pore connectivity, water retention, permeability, and solute transport using network models. *Eur. J. Soil Sci.*, 51, 99-105, 2000.
- Wang, Y., Shao, M., Liu, Z., and Horton, R.: Regional-scale variation and distribution patterns of soil saturated hydraulic conductivities in surface and subsurface layers in the loessial soils of China, *J. Hydrol.*, 487, 13-23, 2013.
- Weynants, M., Vereecken, H., and Javaux, M.: Revisiting Vereecken pedotransfer functions: Introducing a closed-form hydraulic model, *Vadose Zone J.*, 8, 86-95, 2009.
- Wösten, J.H.M., Lilly, A., Nemes, A., and Bas, C.L.: Development and use of a database of hydraulic properties of European soils, *Geoderma*, 90, 169-185, 1999.
- Wildenschild, D., and Sheppard, A.: X-ray imaging and analysis techniques for quantifying pore-scale structure and processes in subsurface porous medium systems, *Adv. Water Resour.*, 51, 217-246, 2013.

1 **Table 1:** Descriptive statistics for selected soil physical properties (no. of samples = 65)

Variable	Minimum	Maximum	Mean	Median	Standard deviation	Skewness	CV %
Clay (g 100g ⁻¹)	14.18	18.93	15.82	15.54	1.36	0.65	9
Silt (g 100g ⁻¹)	23.30	33.32	30.12	30.10	1.66	-1.21	6
Sand (g 100g ⁻¹)	44.89	59.00	50.71	50.72	2.14	0.32	4
Organic matter (g 100g ⁻¹)	2.90	3.75	3.35	3.38	0.20	-0.42	6
Saturated hydraulic conductivity (cm hr ⁻¹)	0.02	418.2	40.15	1.38	89.48	2.84	218
Air permeability at -30 cm, K _a -30, (μm ²)	0.03	109.19	10.87	3.21	22.33	3.03	205
Air permeability at -100 cm, K _a -100, (μm ²)	0.19	151.10	14.72	5.42	27.13	3.26	184
Gas diffusivity at -30 cm, D _p /D ₀ -30	1.0×10^{-4}	1.8×10^{-2}	2.6×10^{-3}	1.7×10^{-3}	3.0×10^{-3}	2.74	123
Gas diffusivity at -100 cm, D _p /D ₀ -100	4.0×10^{-4}	2.5×10^{-2}	5.2×10^{-3}	4.0×10^{-3}	5.0×10^{-3}	2.31	92

2
3
4
5
6
7
8
9
10
11
12
13
14
15
16
17
18
19

Table 2: Partial sill, nugget, range, kriging interpolation model, and root mean square error (RMSE) for semivariograms for each interpolated map. All interpolations were performed with ESRI ArcMap 10.1.

Variable	Partial Sill	Nugget	Range (m)	Model	RMSE
Clay (g 100g ⁻¹)	3.1×10^{-4}	3.6×10^{-5}	179	Gaussian	7.0×10^{-3}
Silt (g 100g ⁻¹)	1.6×10^{-4}	2.2×10^{-4}	200	Gaussian	1.5×10^{-2}
Sand (g 100g ⁻¹)	2.9×10^{-4}	1.8×10^{-4}	61	Spherical	1.7×10^{-2}
Organic matter (g 100g ⁻¹)	3.8×10^{-6}	6.8×10^{-7}	89	Spherical	1.2×10^{-3}
Saturated hydraulic conductivity, K _{sat} (cm hr ⁻¹)	6080	3827	24	Spherical	97.23
Air permeability at -30 cm, K _a -30, (μm ²)	80	459	24	Circular	23.45
Air permeability at -100 cm, K _a -100, (μm ²)	0	753	0	Spherical	27.54
Gas diffusivity at -30 cm, D _p /D ₀ -30	2.7×10^{-6}	1.0×10^{-5}	24	Spherical	3.5×10^{-3}
Gas diffusivity at -100 cm, D _p /D ₀ -100	6.3×10^{-6}	2.1×10^{-5}	30	Circular	5.3×10^{-3}

Table 3: Empirical constants for the Ahuja (1984) model with air-filled porosity at -30 kPa, X-ray CT derived effective percolating macroporosity (EPMP), and total macroporosity (MP) as effective porosity ϕ_e , respectively.

Variable	A	B
ϕ_e = air-filled porosity at -30kPa in the Ahuja (1984) model		
Saturated hydraulic conductivity, K_{sat} (cm hr ⁻¹)	5000	3.2
Air permeability at -30 cm, K_a -30, (μm^2)	5000	3.4
Air permeability at -100 cm, K_a -100, (μm^2)	5000	3.2
Gas diffusivity at -30 cm, D_P/D_0 -30	0.27	2.3
Gas diffusivity at -100 cm, D_P/D_0 -100	0.27	2.0
ϕ_e = effective percolating macroporosity (EPMP) in the Ahuja (1984) model for biopore-dominated flow		
Saturated hydraulic conductivity, K_{sat} (cm hr ⁻¹)	5000	1.15
Air permeability at -30 cm, K_a -30, (μm^2)	5000	1.5
Air permeability at -100 cm, K_a -100, (μm^2)	5000	1.4
Gas diffusivity at -30 cm, D_P/D_0 -30	0.27	1.12
Gas diffusivity at -100 cm, D_P/D_0 -100	0.27	0.98
ϕ_e = total macroporosity (MP) in the Ahuja (1984) model for matrix-dominated flow		
Saturated hydraulic conductivity, K_{sat} (cm hr ⁻¹)	5000	3.2
Air permeability at -30 cm, K_a -30, (μm^2)	5000	3.0
Air permeability at -100 cm, K_a -100, (μm^2)	5000	2.7
Gas diffusivity at -30 cm, D_P/D_0 -30	0.27	1.90
Gas diffusivity at -100 cm, D_P/D_0 -100	0.27	1.55

Figures Captions:

Figure 1: Flowchart illustrating all performed CT-data enhancement, segmentation, and analysis steps.

Figure 2: Contour maps depicting the spatial distribution of soil textural properties and macropore flow parameters; (a) clay ($< 2 \mu\text{m}$), (b) silt ($2 \mu\text{m} - 50 \mu\text{m}$), (c) sand ($50 \mu\text{m} - 2000 \mu\text{m}$), (d) organic matter content, (e) saturated hydraulic conductivity (cm hr^{-1}), (f) air permeability (μm^2) at -100 cm matric potential, and (g) gas diffusivity at -100 cm matric potential. Visualizations of samples marked as *I*, *II*, *III*, and *IV*, are depicted in Figure 3.

Figure 3: Three-dimensional visualizations of sample soil columns and associated measured macropore flow parameters. K_{sat} is saturated hydraulic conductivity, and K_a-100 and D_p/D_0-100 are air permeability and gas diffusivity at -100 cm matric potential, respectively.

Figure 4: Predictive performance of empirical saturated hydraulic conductivity (K_{sat}) models. Filled symbols represent samples with biopore-dominated flow and empty symbols represent samples with matrix-dominated flow. Visualizations of samples marked as *I*, *II*, *III*, and *IV*, are depicted in Figure 3.

Figure 5: Predictive performance of empirical models for air permeability (K_a) and gas diffusivity (D_p/D_0) at -30 cm and -100 cm matric potentials. (a, b) Chamindu Deepagoda et al. (2011) model; (c, d) WLR-Marshall model (Moldrup et al., 2000). Filled symbols represent samples with biopore-dominated flow and empty symbols represent samples with matrix-dominated flow. Visualizations of samples marked as *I*, *II*, *III*, and *IV*, are depicted in Figure 3.

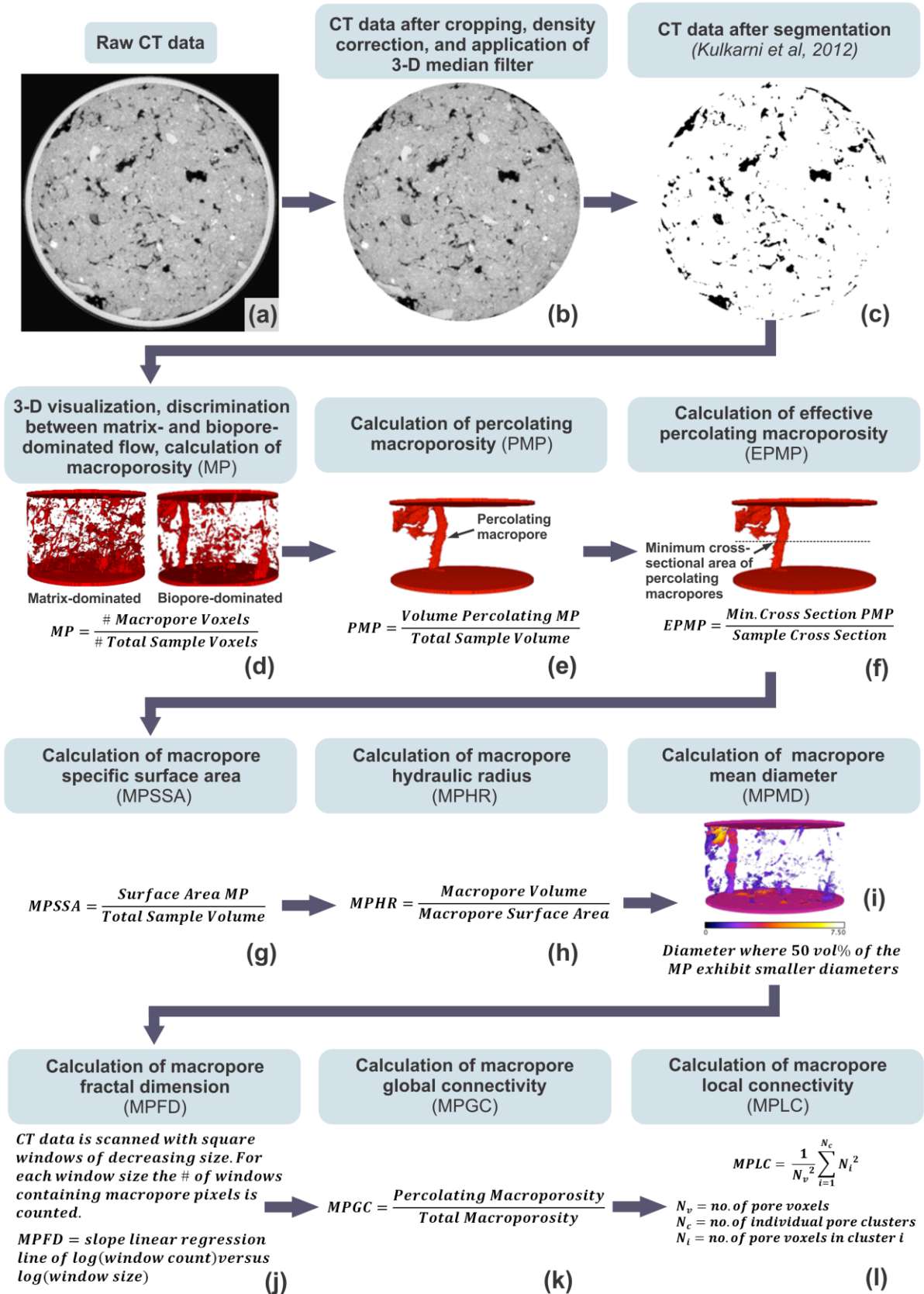
Figure 6: CT-derived macroporosity plotted as a function of physically measured air-filled porosity at -30 cm matric potential.

Figure 7: Spearman rank order correlation analysis for (a) all samples ($n = 65$), (b) samples with biopore flow ($n = 16$), and (c) samples with matrix flow ($n = 49$); stars indicate significant correlations at p value < 0.01 . MP is macroporosity, PMP is percolating macroporosity, EPMP is effective percolating macroporosity, MPSSA is macropore specific surface area, MPHR is macropore hydraulic radius, MPMD is macropore mean diameter, MPFD is macropore fractal dimension, MPGC is macropore global connectivity, MPLC is macropore local connectivity, K_{sat} is saturated hydraulic conductivity (cm hr^{-1}), K_{a-30} is air permeability (μm^2) at -30 cm matric potential, K_{a-100} is air permeability (μm^2) at -100 cm matric potential, D_p/D_0-30 is gas diffusivity at -30 cm matric potential, and D_p/D_0-100 is gas diffusivity at -100 cm matric potential. Strong correlation ($r > 0.70$), moderate correlation ($r = 0.5 - 0.7$), and weak correlation ($r < 0.5$).

Figure 8: Saturated hydraulic conductivity (K_{sat}), air permeability at -30 cm matric potential (K_{a-30}), air permeability at -100 cm matric potential (K_{a-100}), gas diffusivity at -30 cm matric potential (D_p/D_0-30), and gas diffusivity at -100 cm matric potential (D_p/D_0-100) were plotted as a function of selected CT-derived macropore network characteristics; filled symbols represent samples with biopore-dominated flow and empty symbols represent samples with matrix-dominated flow. Fitting linear regression models has been attempted; a power model was always superior where a significant correlation was present. Two separate regressions were fitted for samples with biopore flow and matrix flow if they were significantly different. Plots g, k, l, and p only show one curve because the other was not significant,

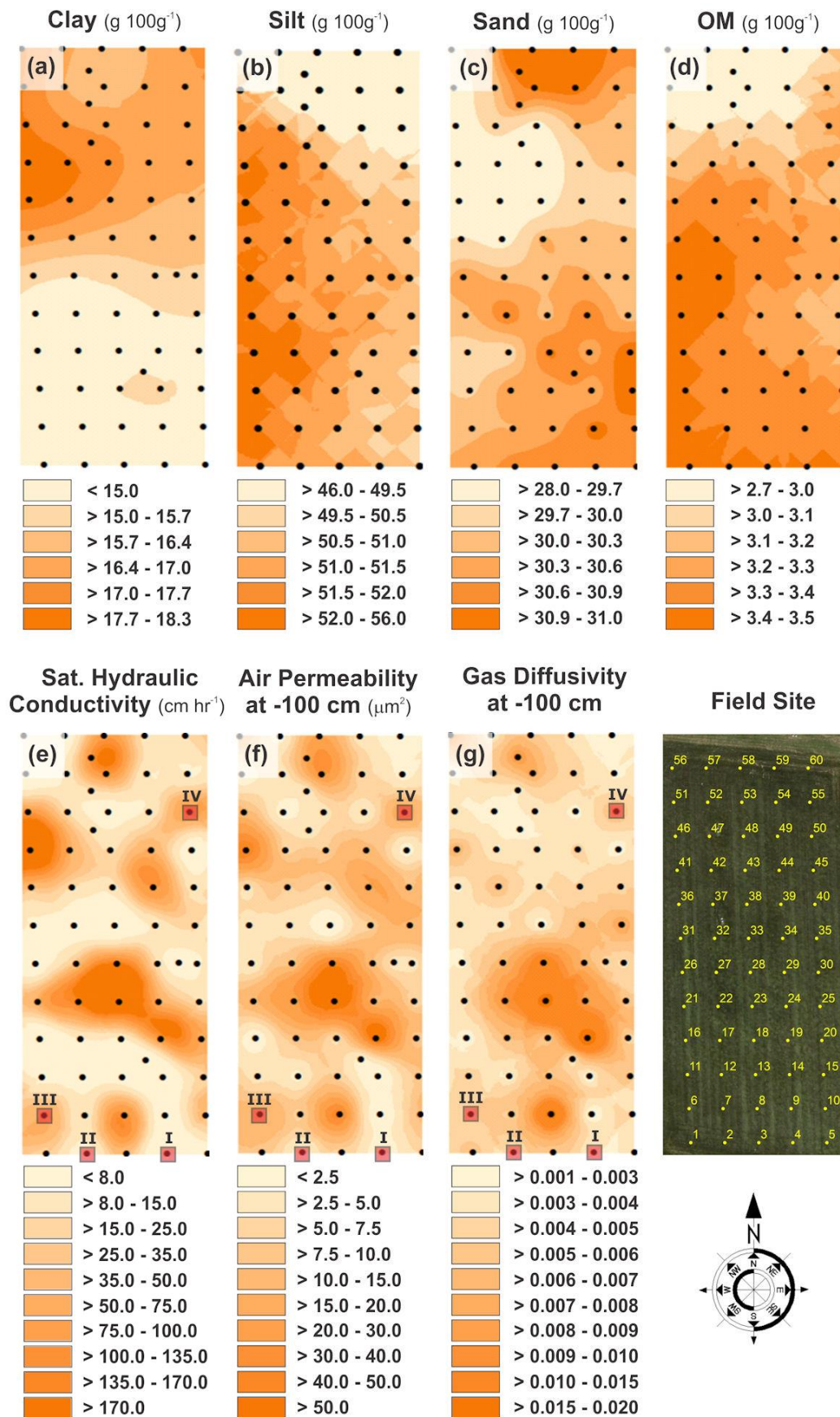
1 while plots q, r, and t have only one model because the two models did not differ
2 significantly from each other.

3 **Figure 9:** Predictive performance of the Ahuja et al. (1984) model parameterized with air-
4 filled porosity at -30 kPa (red empty symbols), X-ray CT derived effective
5 percolating macroporosity (EPMP) (black filled symbols), and total
6 macroporosity (MP) (black empty symbols), respectively. Predicted (a) saturated
7 hydraulic conductivity, (b) air permeability at -30 cm matric potential, (c) air
8 permeability at -100 cm matric potential, (d) gas diffusivity at -30 cm matric
9 potential, and (e) gas diffusivity at -100 cm matric potential.



1

2 Figure 1



1

2 **Figure 2**

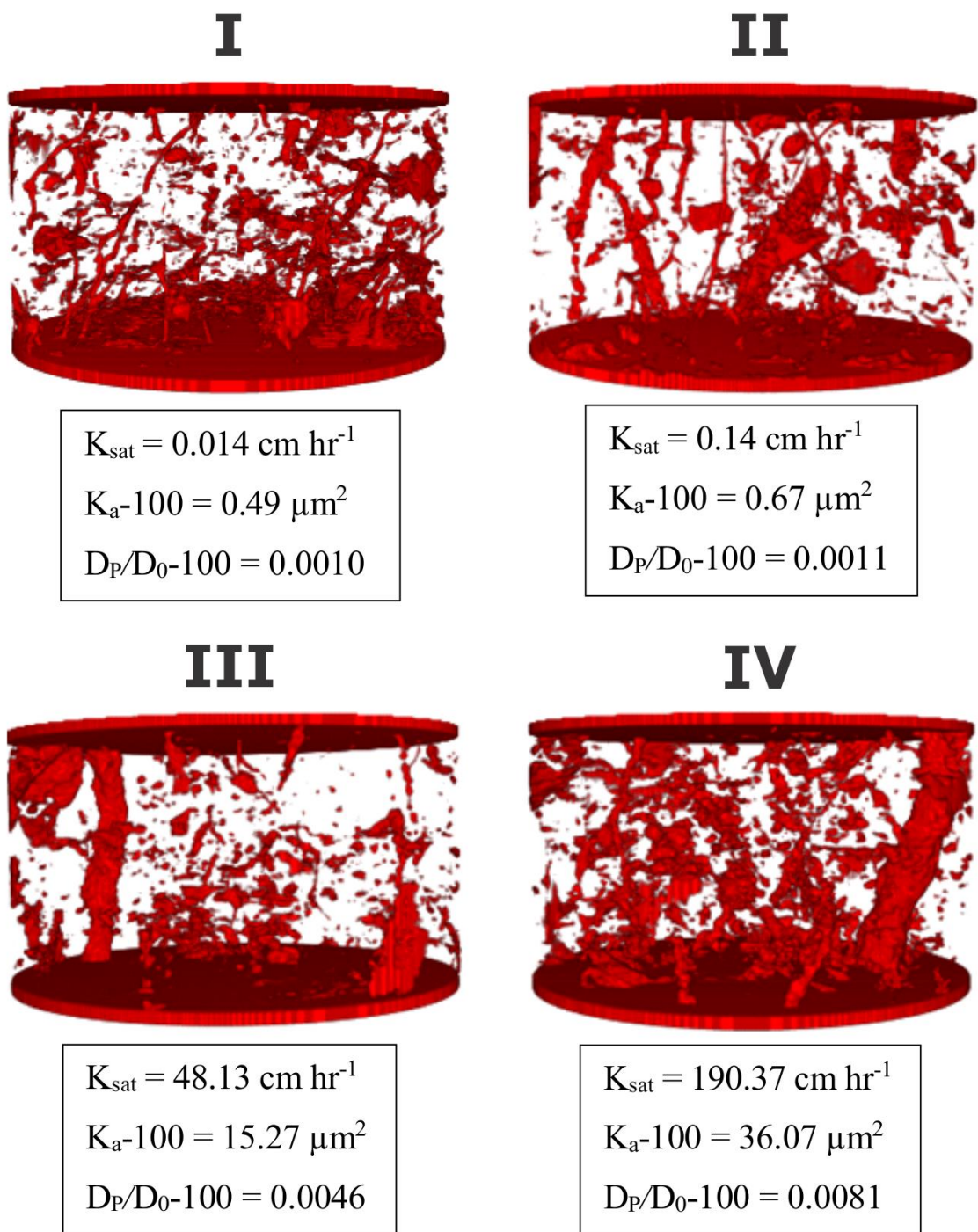


Figure 3

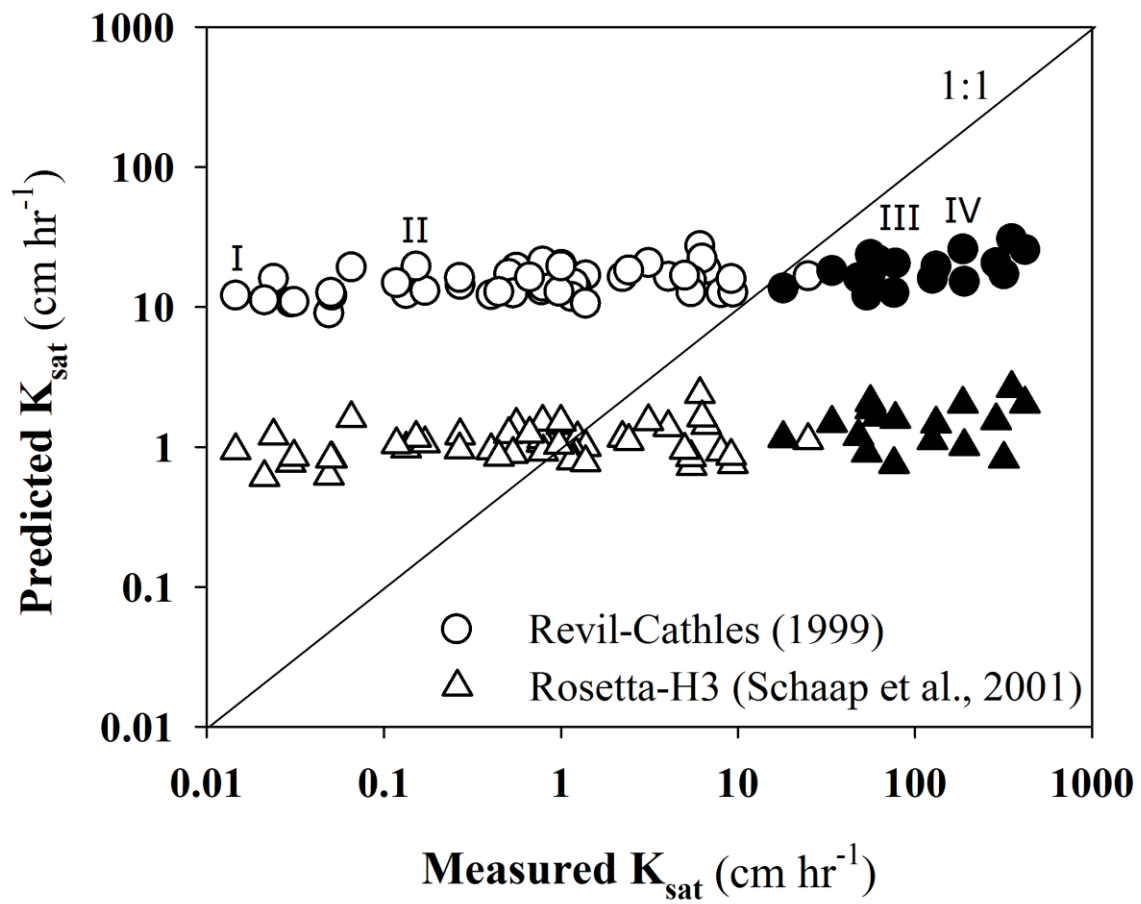


Figure 4

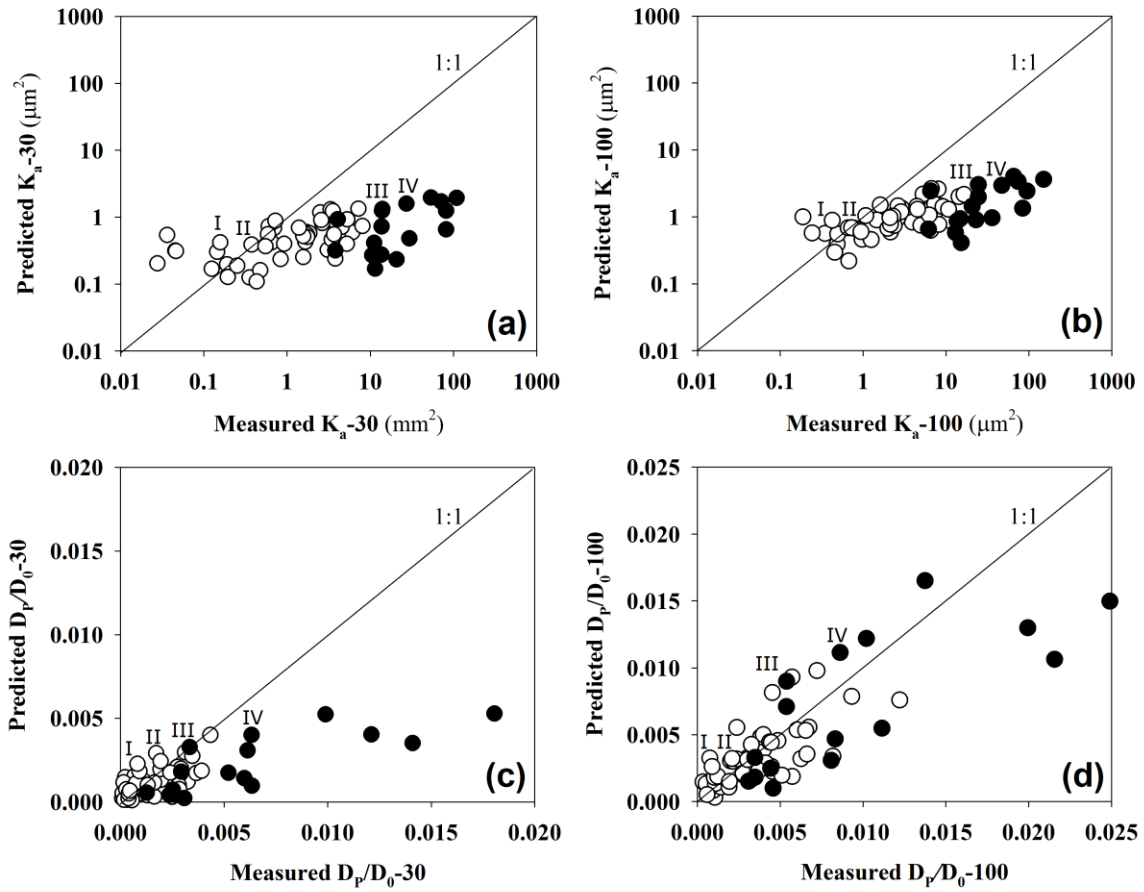


Figure 5

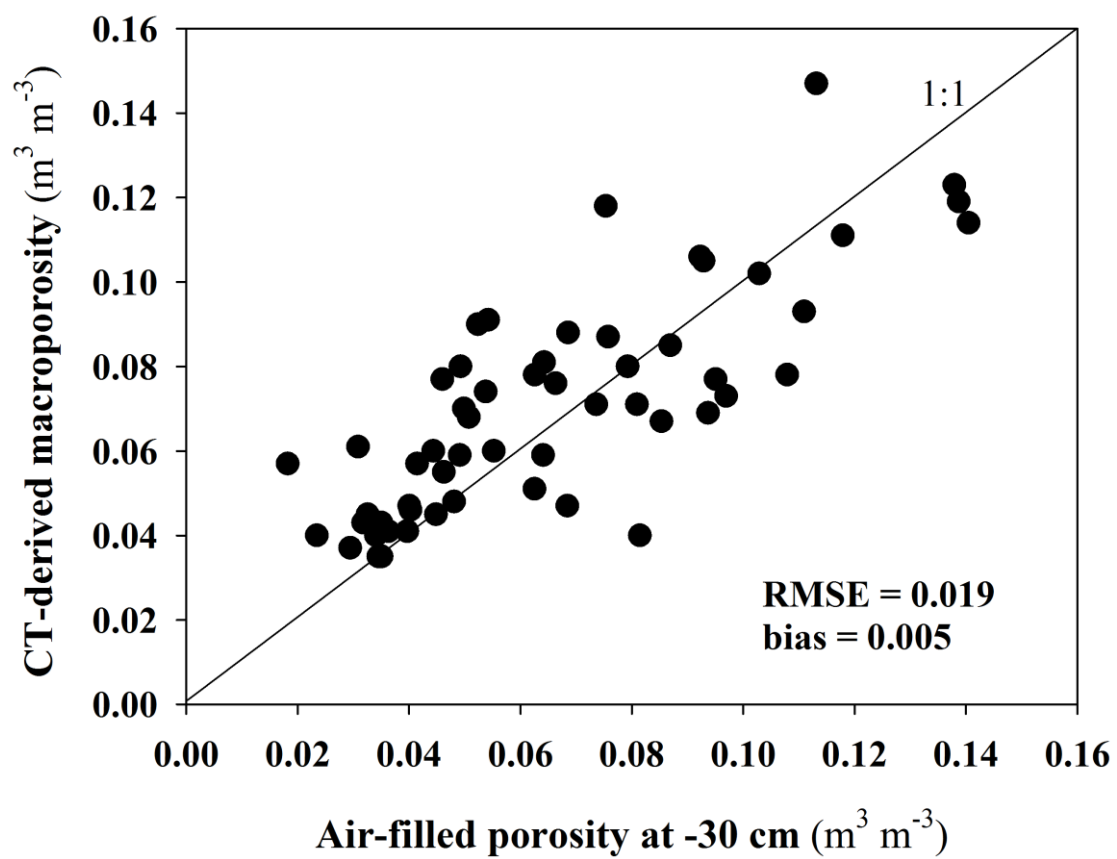
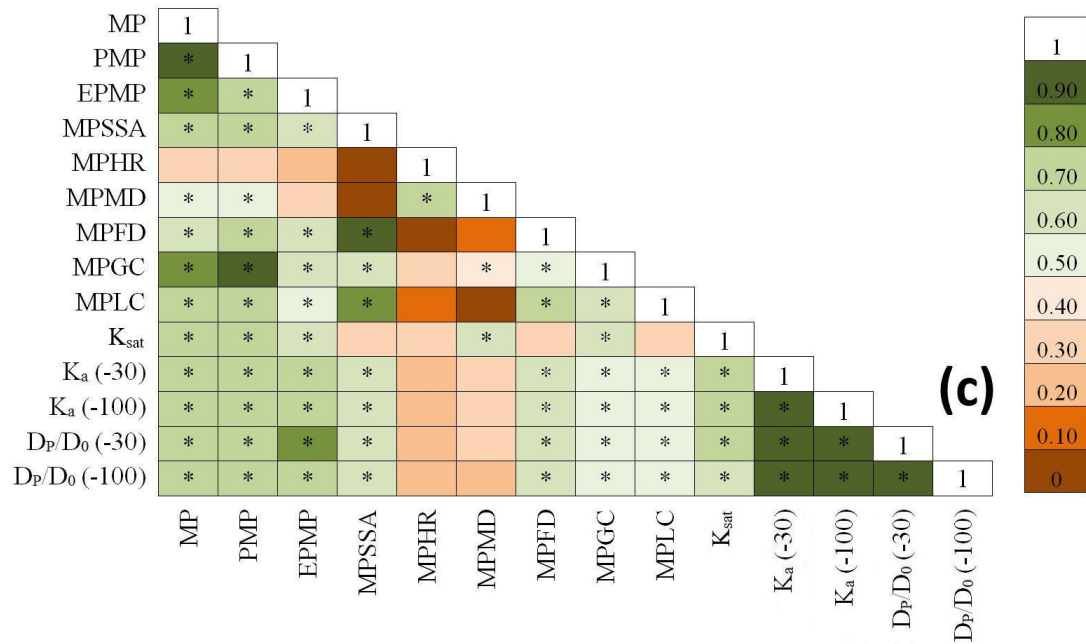
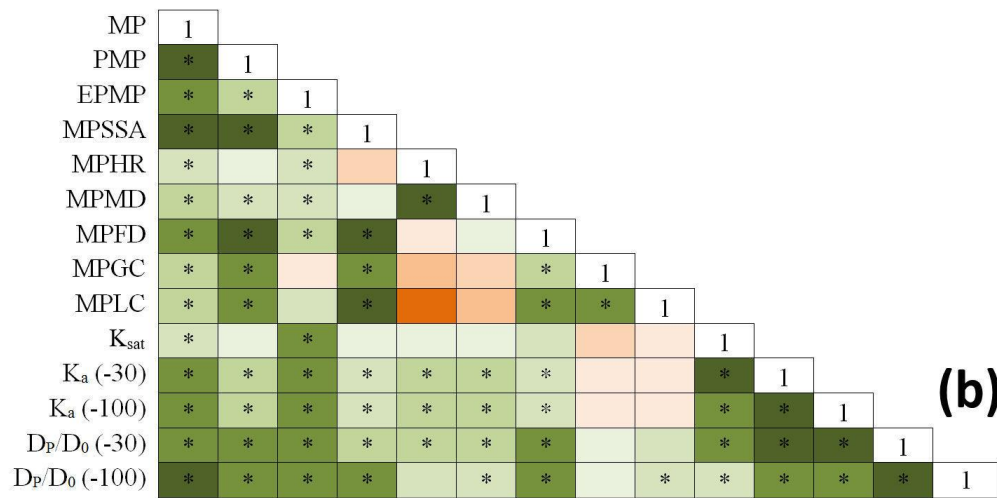
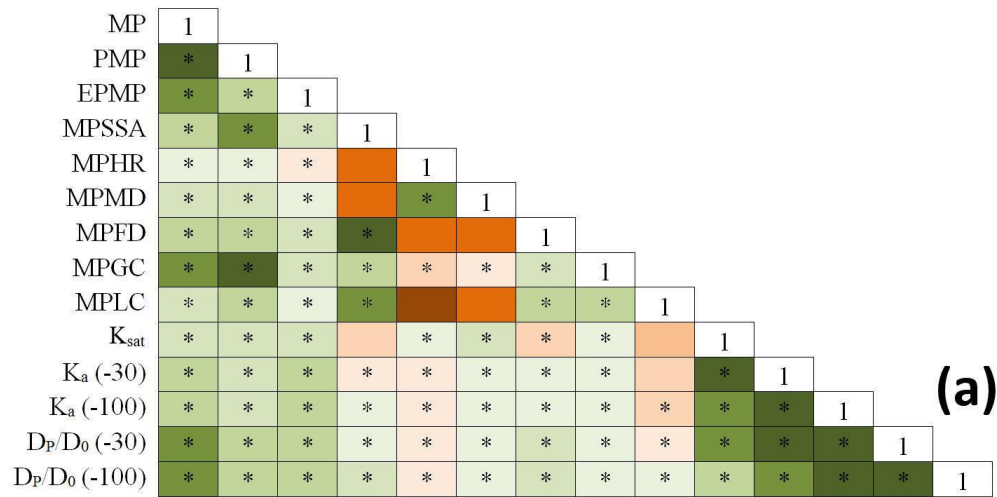


Figure 6



1

2 **Figure 7**

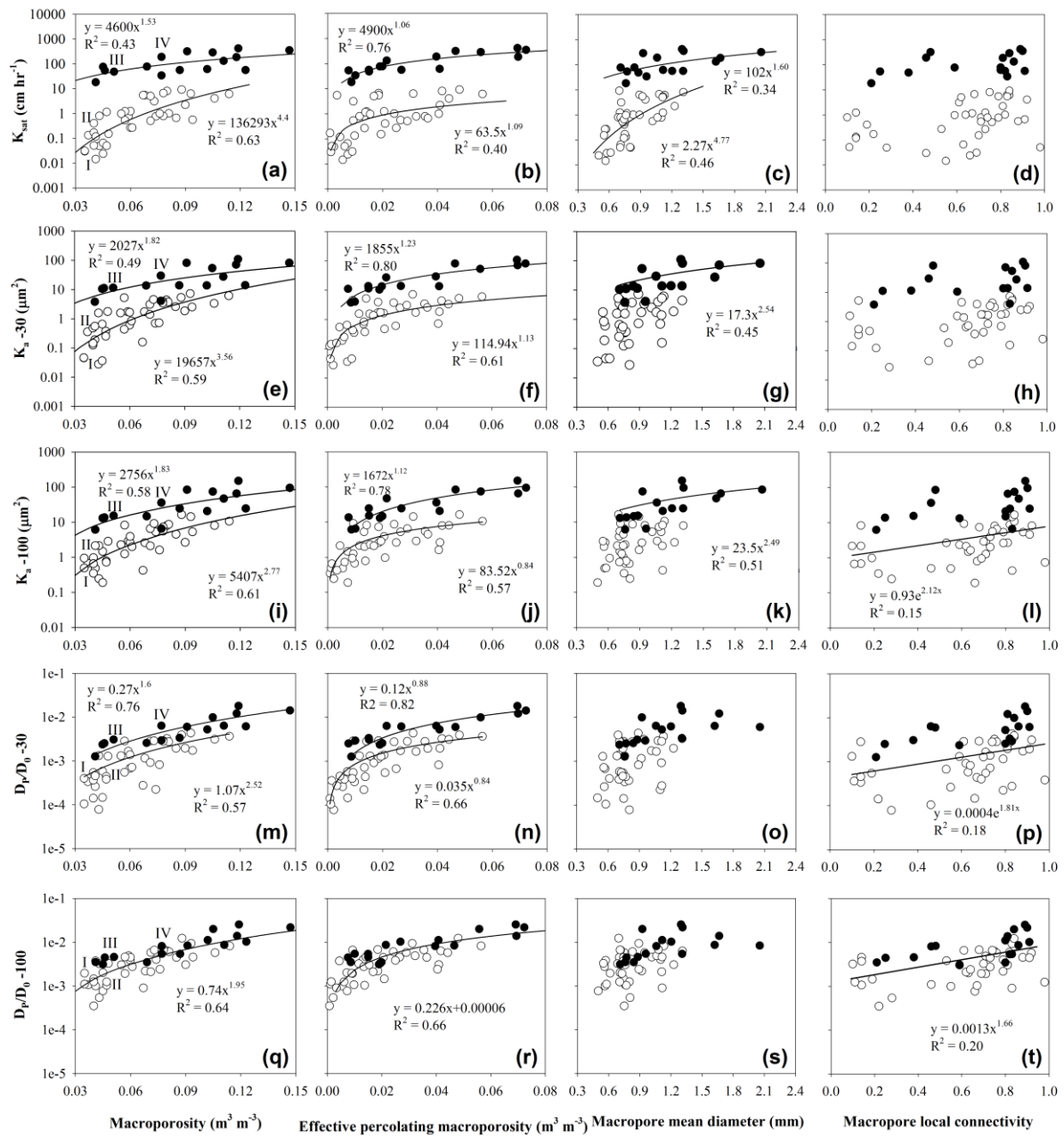
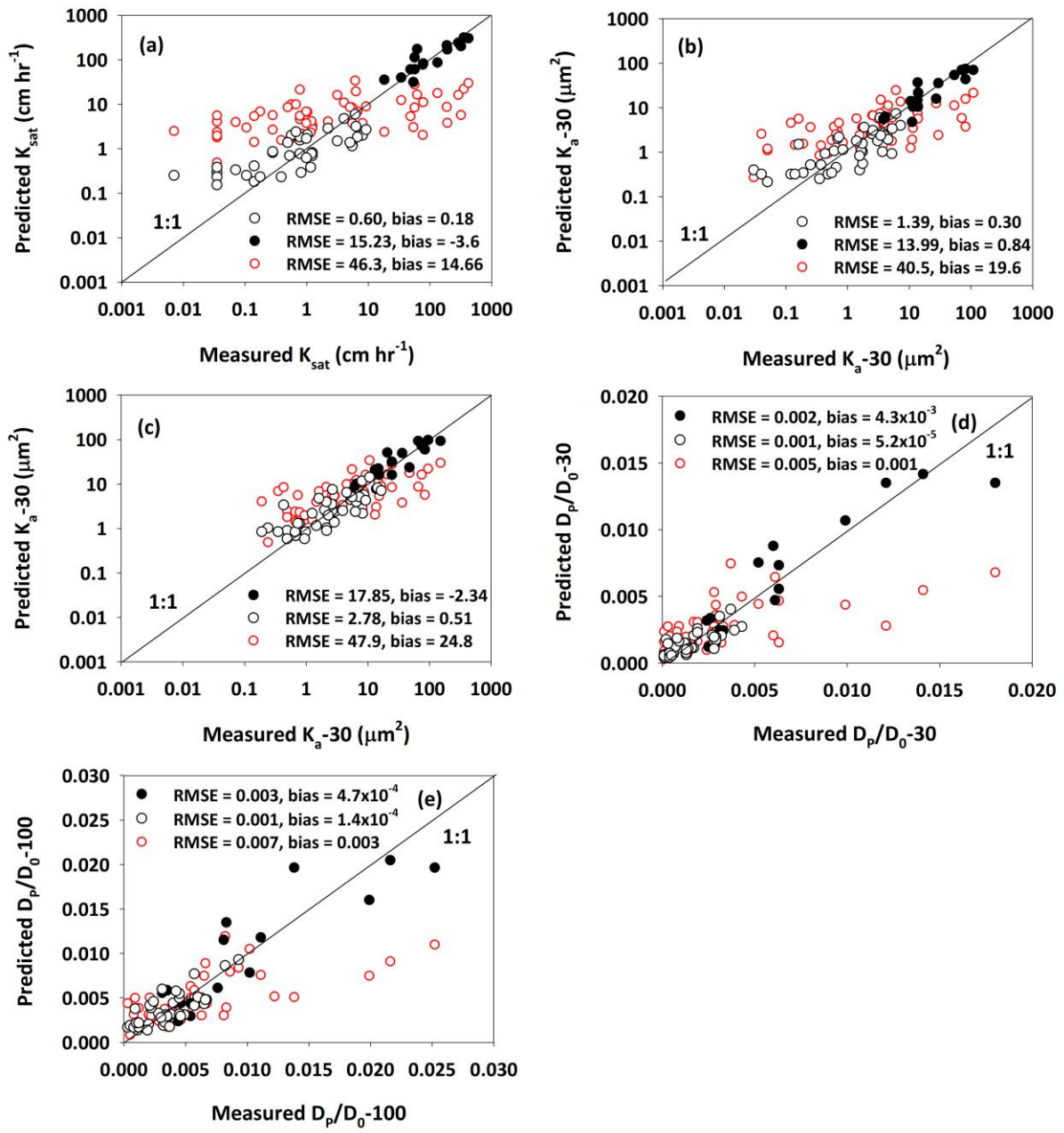


Figure 8



1

2 **Figure 9**